

Galaxy formation in the Planck cosmology II: star-formation histories and post-processing magnitude reconstruction

Sorour Shamshiri¹, Peter A. Thomas^{1*}, Bruno M. Henriques², Rita Tojeiro³, Gerard Lemson^{2,4}, Seb J. Oliver¹, Stephen Wilkins¹

¹*Astronomy Centre, University of Sussex, Falmer, Brighton BN1 9QH, United Kingdom*

²*Max-Planck-Institut für Astrophysik, Karl-Schwarzschild-Str. 1, 85741 Garching b. München, Germany*

³*School of Physics & Astronomy, Physical Science Building, North Haugh, St. Andrews, KY16 9SS, UK*

⁴*Department of Physics & Astronomy, Johns Hopkins University, Baltimore, MD, US, 21218*

Submitted to MNRAS

ABSTRACT

We adapt the L-Galaxies semi-analytic model to follow the star-formation histories (SFH) of galaxies – by which we mean a record of the formation time and metallicities of the stars that are present in each galaxy at a given time. We use these to construct stellar spectra in post-processing, which offers large efficiency savings and allows user-defined spectral bands and dust models to be applied to data stored in the Millennium data repository.

We contrast model SFHs from the Millennium Simulation with observed ones from the VESPA algorithm as applied to the SDSS-7 catalogue. The overall agreement is good, with both simulated and SDSS galaxies showing a steeper SFH with increased stellar mass. The SFHs of blue and red galaxies, however, show poor agreement between data and simulations, which may indicate that the termination of star formation is too abrupt in the models.

The mean star-formation rate (SFR) of model galaxies is well-defined and is accurately modelled by a double power law at all redshifts: $\text{SFR} \propto 1/(x^{-1.39} + x^{1.33})$, where $x = (t_a - t)/3.0$ Gyr, t is the age of the stars and t_a is the lookback time to the onset of galaxy formation; above a redshift of unity, this is well approximated by a gamma function: $\text{SFR} \propto x^{1.5} e^{-x}$, where $x = (t_a - t)/2.0$ Gyr. Individual galaxies, however, show a wide dispersion about this mean. When split by mass, the SFR peaks earlier for high-mass galaxies than for lower-mass ones, and we interpret this downsizing as a mass-dependence in the evolution of the quenched fraction: the SFHs of star-forming galaxies show only a weak mass dependence.

Key words: methods: numerical – galaxies: formation – galaxies: evolution

1 INTRODUCTION

Understanding the astrophysics behind the formation and evolution of galaxies is an important goal in modern astronomy. One of the most fundamental probes of that physics is the star-formation rate as a function of cosmic time. In this paper we contrast predicted and observed star-formation histories (hereafter, SFHs) of galaxies, and explore the expected range of SFHs at high redshift.

Two main observational approaches are used to infer the star formation history of galaxies. One can look at the instantaneous star formation rate as a function of cosmic time (for an overview see, e.g. Kennicutt 1998; Calzetti 1999), or one can deduce the history from the fossil record of current-day galaxies. The two techniques in fact measure slightly different things, with the relationship between the two depending upon the merging history of the galaxies.

This paper focusses upon the archaeological approach. We have extended the L-GALAXIES semi-analytic model (hereafter simply L-GALAXIES) to keep a record of the SFHs of individual galaxies, with a bin-size that increases with increasing age for the stars. The resulting data have been made available as part of the public data release of the Millennium Simulation¹ that accompanies the latest implementation of L-GALAXIES (Henriques et al. 2014).

We note that the SFH as defined in this paper (the history of star formation of all the stars that end up in the galaxy at some particular time) is related to, but distinct from, the variation in mass of a galaxy over time. The latter follows only the history of the main component of the galaxy (along the “main branch” of the merger tree) and has been investigated for the Millennium Simulation by

* E-mail: P.A.Thomas@sussex.ac.uk

¹ <http://gavo.mpa-garching.mpg.de/MyMillennium/>

Cohn & van de Voort (2014). The difference between the two reflects the merger history of galaxies.

The term SFH is often loosely used in papers without being defined. Observationally, the only *direct* measure of SFHs corresponds to that described in this paper, i.e. the distribution of formation times of all the stars that make up the galaxy.² Measures of the SFH of the main galactic component can only be inferred statistically by observing populations of galaxies at different redshifts and making some assumptions about merger rates as a function of stellar mass and environment. In principle, the former method is much cleaner, as it is free from these model assumptions; however, in practice, the inversion of the stellar spectra is highly degenerate and sensitive to the input stellar population synthesis models, and can lead to implausible results if some model constraints are not imposed.

As well as enabling comparison to observations, the introduction of SFHs into L-GALAXIES allows reconstruction of galaxy magnitudes using arbitrary stellar population synthesis and dust models, in any band, in post-processing, and we investigate the accuracy of this approach. In addition, having SFHs is a prerequisite for a correct, time-resolved treatment of galactic chemical enrichment, as described in Yates et al. (2013).

The star-formation history of a galaxy, its chemical evolution, and its current dust content, can in principle be fully recovered with high enough quality observational data, suitable modelling of the spectral energy distribution of stellar populations and dust extinction, and appropriate parametrisation. Several algorithms have been developed over the last decade that attempt to do the above in the most robust way (see e.g. MOPED by Heavens et al. 2004; Panter et al. 2007, STECMAP by Ocvirk et al. 2006, STARLIGHT by Cid Fernandes et al. 2004, 2005 or ULySS by Koleva et al. 2009). In this paper we focus on the results obtained by VESPA Tojeiro et al. (2007), a full spectral fitting code that was applied to over 800,000 Sloan Digital Sky Survey Data-Release 7 galaxies (?). The resulting database of individual star-formation histories, metallicity histories and dust content is publicly available and described in Tojeiro et al. (2009) (hereafter TWH09). The wide range of galaxies in SDSS DR7 and the time-resolution of the SFHs published in the database make it ideal for a detailed comparison with our model predictions.

At higher redshift, observational data are scarce. Nevertheless, we make predictions from our models of how the star-formation rate of galaxies evolves with redshift, and we show how down-sizing arises from a mass-dependence of the rate at which galaxies are quenched.

In outline, the main aims of this paper are:

- to briefly overview the L-GALAXIES and VESPA algorithms – Sections 2.1 & 2.2;
- to describe the L-GALAXIES SFH binning method – Section 2.3;
- to test how well post-processing can reconstruct magnitudes – Section 3;
- to compare model galaxies from L-GALAXIES with results from the VESPA catalogue – Section 4;
- to investigate the variety of SFHs that we find in our model galaxies – Section 5;
- to provide a summary of our key results – Section 6.

² We note that this would better be described by the phrase “stellar age distribution” rather than star-formation history, but the latter phrase predominates in the literature.

2 METHODS

2.1 L-GALAXIES

In this work we use the latest version of the Munich semi-analytic (SA) model, L-GALAXIES, as described in Henriques et al. (2014). This gives a good fit to, amongst other things, the observed evolution of the mass and luminosity functions of galaxies, the fraction of quenched galaxies, the star-formation vs stellar mass relation (at least at $z < 2$), the Tully-Fisher relation, metallicities, black-hole masses, etc. We refer to this standard model as HWT14. The improvements obtained in terms of the evolution of the abundance and red fractions of galaxies as a function of stellar mass in this model result from: a supernova feedback model in which ejected gas is allowed to fall back onto the galaxy on a timescale that scales inversely with halo virial mass (Henriques et al. 2013); and a lower star formation threshold and weaker environmental effects both reducing the suppression of star formation in dwarf galaxies.

L-GALAXIES, as with other SA models, follows the growth of galaxies within the framework of a merger tree of dark matter halos. We construct this tree from the Millennium Simulation (Springel et al. 2005), scaled using the method of Angulo & White (2010) to the Planck Cosmology (Collaboration & et al. 2013): $\Omega_m = 0.315$, $\Omega_\Lambda = 0.683$, $\Omega_b = 0.0488$, $n_s = 0.958$, $\sigma_8 = 0.826$, $h = 0.673$. This then gives a box size of $480.3 h^{-1}$ Mpc and a particle mass of $9.61 \times 10^8 h^{-1} M_\odot$. The merger tree is constructed from 58 snapshots,³ each of which is subdivided into 20 integration timesteps. The snapshots are unevenly spaced, such that the time-resolution is higher at high redshift, but a typical timestep is of order $1-2 \times 10^7$ yr. We note that the SA model has been implemented on both the higher resolution Millennium-II (Boylan-Kolchin et al. 2009) and larger volume Millennium-XXL simulations (Angulo et al. 2014) although we do not make use of those simulations in the current work.

Prior to HWT14, galaxy luminosities were determined by accumulating flux in different spectral bands throughout the time-evolution of each galaxy. In the new model those fluxes are recovered to high accuracy in post-processing, by simply recording the star-formation and metallicity history in a relatively small number of time-bins. The new method is introduced following the work outlined and presented in the current paper. The data release that accompanies this series of papers records the star-formation histories, allowing the user flexibility to define their own bands and dust models.

2.2 VESPA

The spectrum of galaxy, in the absence of dust, can be described as the linear superposition of the spectra of the stellar populations of different ages and metallicities that exist in the galaxy. The deconvolution of a galaxy’s spectrum into a star-formation and metallicity history is in principle trivial, but complicated by noisy or incomplete data and limitations in the modelling. Ocvirk et al. (2006) showed how the problem quickly becomes ill-conditioned as noise increases in the data, and that the risk of over-parametrizing a galaxy is high. VESPA takes into account the noise and data quality of each individual galaxy and uses an algebraic approach to estimate how many linearly independent components one can extract

³ 5 of the original *Millennium Simulation* snapshots lie at $z < 0$ after scaling.

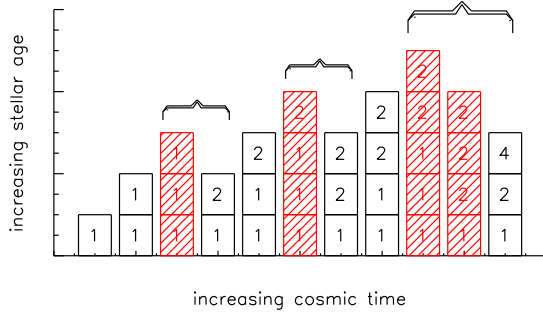


Figure 1. The evolution of the SFH bins for $N_{\max} = 2$. The x -axis represents successive timesteps, starting from high redshift and moving towards the present day. The y -axis represents bins of stellar age, starting with stars that are newly-created at that time and looking back into the past. The numbers within each bin represent the number of timesteps that have been merged together to produce that bin. The columns that are bracketed together show different arrangements of the data at a single cosmic time. The shaded, red stacks represent transient structures in which some bins merge together to produce the black stacks to their right.

from each observed spectrum, thereby avoiding fitting the noise rather than the signal - see Tojeiro et al. (2007) for details.

VESPA recovers the star-formation history of a galaxy in 3 to 16 age bins (depending on the quality of the spectra), logarithmically spaced between 0.002 Gyr and the age of Universe. For each age bin, VESPA returns the total mass formed within the bin and a mass-weighted metallicity of the bin, together with an estimate of the dust content of the galaxy. As we always compare our model predictions to the mean SFH of large ensembles of galaxies, we choose to use the fully-resolved SFHs published in the database of TWH09. Whereas we expect these to be dominated by the noise on each individual galaxy, the mean over a large ensemble has been shown to be robust (Panter et al. 2003). In this paper, we will compare to mean SFHs for different galaxy populations, as described in the text.

2.3 The SFH binning algorithm

As mentioned in Section 2.1, the Millennium merger trees are constructed from 58 snapshots, each of which is separated into 20 integration timesteps. To follow the history of star-formation, we introduce extra arrays to carry information on the mass and metallicity of stars in each component of the galaxy (disk, bulge, intracluster mass) as a function of cosmic time. To save the information over all 1160 timesteps would consume too much memory and is unnecessary. Instead, we wish to use a high resolution for the recent past (when the stellar population is rapidly evolving) and a lower one at more distant times. To do so, we adopt the following procedure (see Figure 1).

Starting at high redshift, on each timestep a new bin is created to hold the star-formation history information. Whenever the number of bins of a particular resolution exceeds N_{\max} (where in the diagram, for the purposes of illustration, $N_{\max} = 2$), then the two oldest bins are merged together to form a new bin of twice the size – this may result in a cascade of mergers at successively higher levels

Table 1. For the *Millennium Simulation*, using 1160 timesteps, this table shows, for different choices of N_{\max} : N_{tot} – the maximum number of SFH bins required; $N_{z=0}$ – the number of populated bins at $z = 0$; $\Delta t_{\text{min}}/\text{yr}$ – the minimum bin-size in years at $z = 0$; $\Delta t_{\text{max}}/\text{yr}$ – the maximum bin-size in years at $z = 0$.

N_{\max}	N_{tot}	$N_{z=0}$	$\Delta t_{\text{min}}/\text{yr}$	$\Delta t_{\text{max}}/\text{yr}$
1	11	7	6.0×10^7	1.1×10^{10}
2	19	16	1.5×10^7	2.1×10^9
3	27	23	1.5×10^7	1.6×10^9
4	34	31	1.5×10^7	5.6×10^8

(in the figure, these mergers are represented by red columns joined by braces to the merger product). In this way, the number of bins at each size grows from 1 to N_{\max} , then oscillates between N_{\max} and $N_{\max} - 1$. The total number of bins required does not exceed the smallest integer greater than $N_{\max} \log_2(N_{\text{step}}/N_{\max} + 1)$, where N_{step} is the number of timesteps. Table 1 shows, for the *Millennium Simulation*, using 20 steps within each of 58 snapshots, the maximum number of bins required, and, at $z = 0$, the actual number of SFH bins and their minimum and maximum size in years.⁴ Note that all choices of $N_{\max} \geq 2$ have the same minimum bin-size, equal to that of the original timesteps; what differs is the number of bins that are resolved at that highest resolution.

We have investigated the sensitivity of our results to the number of bins and conclude that $N_{\max} = 2$ gives the best balance between data-size and accuracy: that is the value used in the Millennium database and, unless mentioned otherwise, in the results presented below.

3 POST-PROCESSING OF MAGNITUDES

In most SA models, and in L-GALAXIES prior to this work, galaxy luminosities are computed by adding the flux in different bands throughout the time-evolution of each galaxy. This calculation generally requires interpolating between values in large stellar population synthesis tables and represents a large fraction, and in some cases the majority, of the computational time for the entire galaxy formation model. The problem is aggravated as different types of magnitudes (dust corrected, observer-frame) for additional components (e.g. disk, bulge, intra-cluster light) are included.

These difficulties can, in principle, be circumvented by storing the star formation and metallicity histories for different components of the galaxies, and using them to compute emission in post-processing. Ideally, this history would be stored for all the intermediate steps between output snapshots for which galaxy properties are computed. However, memory constraints make this infeasible. For our current set up, for example, it would require storage of up to 2320 values for each galaxy component (58 snapshots, 20 intermediate steps per snapshot, star formation and metallicity).

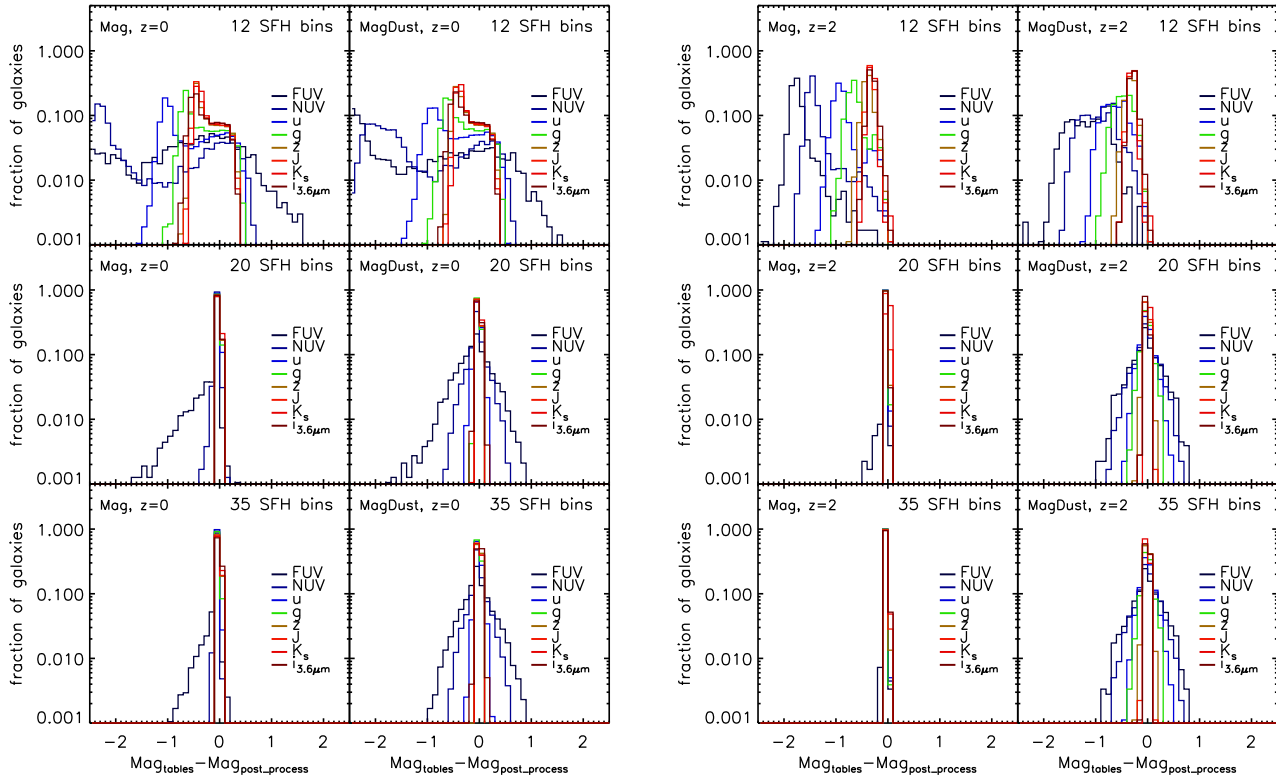
An alternative, tested in this paper, is to store the histories in bins that grow in size for older populations, as described in Section 2.3. Since the emission properties of populations vary on significantly longer time-scales for old populations this can in principle allow us to maintain accuracy. To validate the method we compare the theoretical emission from galaxies computed both with full

⁴ These numbers are unchanged for the 63 snapshots required to use the *Millennium Simulation* with the original WMAP-1 cosmology.

Table 2. This table shows the root-mean-square difference between magnitudes calculated on-the-fly during the running of the code and those calculated in post-processing.

$z = 0$	without dust			with dust		
	$N_{\max} = 1$	$N_{\max} = 2$	$N_{\max} = 4$	$N_{\max} = 1$	$N_{\max} = 2$	$N_{\max} = 4$
GALEX <i>FUV</i>	3.02	0.29	0.16	2.53	0.38	0.29
GALEX <i>NUV</i>	1.79	0.05	0.03	1.47	0.16	0.16
SDSS <i>u</i>	0.76	0.03	0.01	0.66	0.06	0.05
SDSS <i>g</i>	0.50	0.02	0.00	0.46	0.03	0.02
SDSS <i>z</i>	0.36	0.02	0.00	0.33	0.02	0.02
VISTA <i>J</i>	0.35	0.02	0.00	0.32	0.02	0.02
VISTA K_s	0.33	0.01	0.01	0.31	0.02	0.02
IRAC $3.6_{\mu\text{m}}$	0.38	0.01	0.00	0.36	0.03	0.02

$z = 2$	without dust			with dust		
	$N_{\max} = 1$	$N_{\max} = 2$	$N_{\max} = 4$	$N_{\max} = 1$	$N_{\max} = 2$	$N_{\max} = 4$
GALEX <i>FUV</i>	1.74	0.04	0.01	1.14	0.27	0.26
GALEX <i>NUV</i>	1.39	0.02	0.00	0.95	0.21	0.20
SDSS <i>u</i>	0.88	0.02	0.00	0.63	0.13	0.12
SDSS <i>g</i>	0.64	0.01	0.00	0.47	0.09	0.09
SDSS <i>z</i>	0.39	0.01	0.00	0.33	0.04	0.04
VISTA <i>J</i>	0.33	0.01	0.00	0.30	0.02	0.02
VISTA K_s	0.32	0.01	0.00	0.30	0.01	0.01
IRAC $3.6_{\mu\text{m}}$	0.31	0.01	0.00	0.28	0.02	0.02

**Figure 2.** The difference between photometric properties calculated using full resolution and binned star formation histories at $z = 0$ (left) and $z = 2$ (right). The left column in each set of panels correspond to intrinsic magnitudes while the right takes into account dust extinction. From top to bottom the resolution of the binning is increased: $N_{\max} = 1$ (top), 2 (middle) & 4 (bottom).

resolution on-the-fly and from star formation and metallicity history bins that are merged together for older populations. We assume that star-formation occurs at a time corresponding to the mid-point of each SFH bin. To spread star-formation out over the time-bin would be equivalent to using a larger number of timesteps (which we have also tested) and makes little difference except in the UV.

Figure 2 shows the difference between photometric properties calculated using full resolution and binned star-formation histories for $z = 0$ and $z = 2$. In both sets of panels the left column corresponds to intrinsic magnitudes while the right column takes into account dust extinction. From top to bottom the resolution of the binning is increased: $N_{\max} = 1, 2 \& 4$. While large differences between the two methods are seen for the lowest resolution, the figures show that good convergence is achieved for $N_{\max} = 2$ or more.

Table 2 shows the root-mean-square difference between magnitudes calculated on-the-fly during the running of the code (i.e. using the finest possible time resolution) and those calculated in post-processing, using different numbers of SFH bins. Quantitatively, for $N_{\max} = 2$, at $z = 0$, the rms difference between the two methods is less than 0.05 for all intrinsic magnitudes except the far-UV, for which it is approximately 0.29.⁵ At $z = 2$, the mean difference is less than 0.04 in all bands.

The increased accuracy in the far-UV at high redshift results from the higher accuracy in post-processing at a time in which fewer bins were merged. Emission in this part of the spectrum is dominated by extremely young populations for which even a slightly different formation time results in a large variation in predicted flux. The two methods thus differ in detail, but have the same statistical properties. If one is interested in the precise UV flux of a particular galaxy then that can be recovered by using finer time-bins. We have checked that, keeping $N_{\max} = 2$ but using a finer timestep (which adds very few SFH bins) improves the agreement between the two methods of calculating fluxes.⁶

At low redshift, it can be seen that there is a residual error in the calculated intrinsic far-UV flux even for $N_{\max} = 4$. This arises from stars of age about 1 Gyr (i.e. the TP-AGB population), for which the tabulated UV fluxes in the Maraston (2005) population synthesis tables show a large jump in luminosity between the two lowest-metallicity bins. Merging galaxies that contain stars of differing metallicity can therefore lead to large changes in flux. Such merging can occur for any choice of N_{\max} and is hence a fundamental (albeit very minor) limitation of the SFH magnitude-reconstruction method.⁷

The addition of dust significantly degrades the agreement between the two reconstruction methods in all bands, with the far- and near-UV being most affected. At $z = 2$ the rms differences between dust-corrected magnitudes are approximately 0.20 for far- and near-UV, 0.10 for u and g , 0.04 for z and J , and 0.02 for K_s and $irac_{3.6\mu m}$.

In the current version of L-GALAXIES a two-component dust model applies extinction separately from the diffuse interstellar medium and from molecular birth clouds (see Section 1.14 in the

supplementary material of Henriques et al. 2014 for details). The large differences seen for dust corrected magnitudes are mostly caused by the latter. The calculation of this optical depth includes a random gaussian term that leads to differences in the amount extinction assumed for each individual galaxy when a different number of timesteps are used.

The method successfully tested in this section is adopted in the recent major release of the Munich model, HWT14. By computing emission properties in post-processing, the memory consumption of the code is no longer dependent on the number of photometric bands. Moreover, *the method allows emission properties to be computed after the model is completed using any stellar populations synthesis code and for the filters used by any observational instrument*. To show the potential of the new method, the new major release already includes emission in 20 bands in the snapshot catalogues, and in 40 bands and for two different stellar populations for the lightcones, all calculated in post-processing.

4 COMPARISON OF VESPA AND L-GALAXIES

For reasons described in Appendix A, we use the version of the VESPA catalogue that was created using the population synthesis model of Maraston (2005) with a 1-component dust model.

Note that the VESPA data and the SA models produce output with very different binning. The time-resolution in the observations is necessarily very coarse at high redshift, whereas there is no such restriction in the models. In Section 4.1 below, we re-bin the model predictions to match those of VESPA; throughout the rest of the paper, we will keep the actual binning returned by the models so as to allow a clearer understanding of the growth of galaxies at high redshift.

4.1 The main galaxy sample

The main SDSS galaxy sample covers a redshift range of $0 < z \lesssim 0.35$. In Fig. 3 we show the mean SFH for all galaxies using the maximum VESPA resolution of 16 bins. For most galaxies, the data quality is not good enough to independently measure masses in all 16 bins and so the VESPA algorithm will return solutions on bins of varying and lower-resolution width, as described in TWH09. The assumed star-formation rate (hereafter, SFR) within each bin depends on its width (it is constant in high-resolution bins, and exponentially decaying in low-resolution bins). Choosing a SFR within a bin is an unavoidable part of the process of parametrizing a galaxy. We have however checked that our conclusions remain unchanged if we: (i) use only galaxies with high-resolution bins, and (ii) use a constant SFR in wide bins.

For each VESPA galaxy, we select the model galaxy that most closely matches it in mass and redshift, then use this to construct a mean star-formation history. The result is shown in Figure 3 along with the predictions from two versions of L-GALAXIES: GWB11–Guo et al. (2011, magenta diamonds and dot-dashed line) and HWT14–Henriques et al. (2014, green squares and dashed lines).

In this and subsequent plots, Δf is defined as the fraction of stars (i.e. the specific stellar mass) within each bin. Unless mentioned otherwise, Δf is calculated separately for each galaxy and then averaged (i.e. weighted by galaxy number rather than stellar mass).

The VESPA results are not as smooth as the SA model data. We expect the averaged rest-frame SFH of a varied ensemble of galaxies to be devoid of significant structure, and to appear smooth

⁵ These values are reduced to 0.03 and 0.16, respectively, when $N_{\max} = 4$ is used.

⁶ We do not use a finer time resolution as a default as this agreement is illusory – the underlying merger tree is not capturing the dynamics on that short a timescale.

⁷ The limitation could be overcome by keeping SFHs for several different metallicity bins, but this moves away from the spirit of the method and we do not think that the gain justifies the extra storage cost.

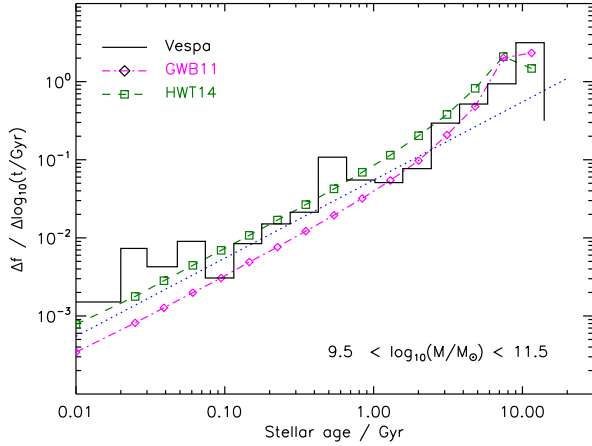


Figure 3. The average SFH from VESPA (black lines), the GWB11 model (magenta, dash-dotted lines) and the HWT14 model (dashed, green lines) within the indicated mass range. To guide the eye, the blue, dotted line is the same in each panel and has slope unity, corresponding to a constant SFR.

as seen on the model galaxies. At late times, especially, the SFR should be approximately constant, and so one would expect the SFH bins to run parallel to the dotted line, of slope equal to unity. The features seen on the data are heavily dependent on the modelling (see e.g. TWH09, Tojeiro et al. 2013, Appendix A), and therefore are the likely result of limitations of the stellar population synthesis and dust modelling.

The SA models show a turn-down in SFR in the oldest stellar age bin, corresponding to the onset of star-formation. No such feature is seen in the VESPA results, most probably because the spectral signatures are too weak to be detected and so the reconstruction method imposes a declining SFR even at these earliest times.

Other than that, at ages above 1 Gyr the GWB11 model seems to provide a reasonable match the observations, whereas for younger stars, the HWT14 model is a better fit. To draw more definitive conclusions about which is the preferred model, one would have to look in much more detail at the reconstruction biases that may be present in the VESPA method when applied to imperfect data, and that will be the subject of future work.

From here on we will rebin the VESPA solutions to 5 bins in age, to reduce the scatter and to average over these features that we know to be unphysical.

4.2 Mass selection

Figure 4 shows the SFHs broken down by stellar mass. The VESPA reconstruction gives a slope that is too steep for high-mass galaxies and too shallow for low-mass galaxies, when compared to the expected constant SFR at recent times. Nevertheless, it can be seen that both the VESPA galaxies, and those in the SA model, form stars earlier in higher-mass galaxies and have a correspondingly lower SFR at late times.

The variation of the model SFHs with mass is explored further in Section 5.3, below.

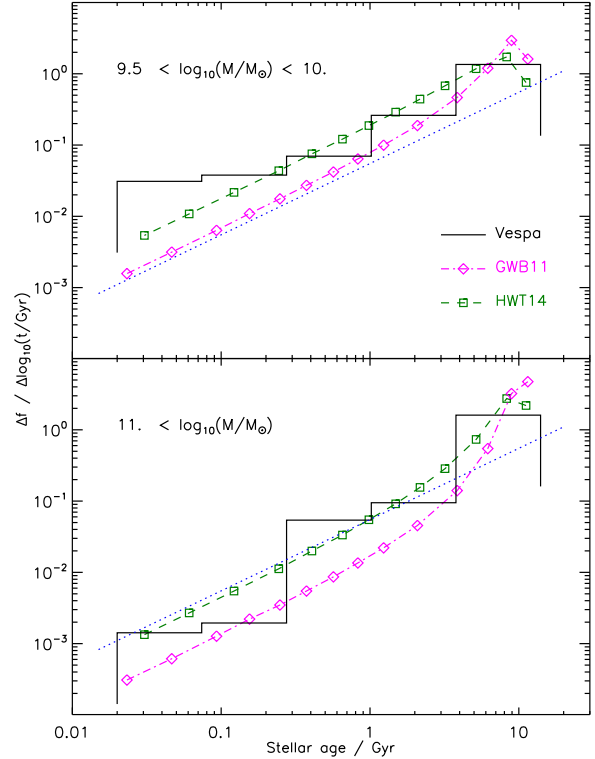


Figure 4. The average SFH from VESPA (black lines), the GWB11 model (magenta, dash-dotted lines) and the HWT14 model (dashed, green lines) within two different stellar mass bins, as shown. To guide the eye, the blue, dotted line is the same in each panel and has slope unity, corresponding to a constant SFR.

4.3 Colour selection

Next, we look at the distinction between red and blue galaxies by selecting according to $u - r$ colour. As HWT14 showed, in spite of reproducing the observed galaxy colour bimodality, L-GALAXIES does not reproduce the exact colour distributions seen in SDSS. Therefore, applying the same colour cuts in the data and simulation would result in picking out intrinsically different galaxy populations. Instead, we select the 10% bluest and reddest galaxies, according to $u - r$ colour, in both the VESPA and L-GALAXIES samples. The resulting SFHs are shown in Figure 5 for galaxies of mass $10^{10} < M / M_{\odot} < 10^{10.5}$ at low redshift, $z < 0.07$.

VESPA produces similar SFHs for both blue and red galaxies except for the youngest stars of age less than 3×10^8 yr. At first sight, it seems surprising that the deviation between the two populations can have occurred so recently. One interpretation is that galaxies in this mass range may transition back and forth between star-forming and quiescent (i.e. show bursts of star formation) on timescales of this order, and that might also help to explain why the SFR of the bluest galaxies seems to increase to the present day. However, this seems at odds with the observation that red and blue galaxies are observed to have very different metallicities: the stellar-mass-weighted metallicity of the young (age less than 2.5

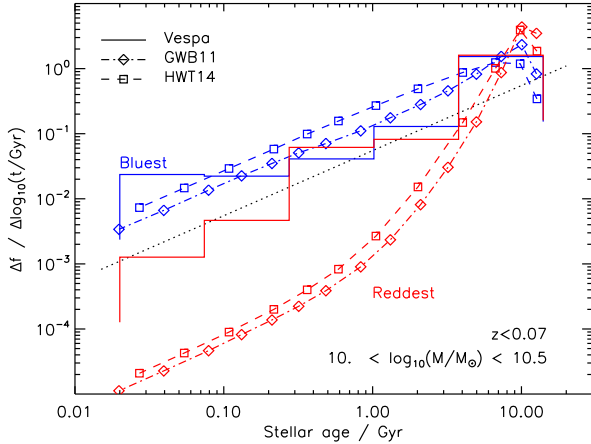


Figure 5. The averaged star formation history from VESPA (solid lines), the GWB11 models (dashed-dotted lines), and the HWT14 model (dashed lines) for red and blue galaxies with masses greater than $10^{11} M_{\odot}$ and within redshift interval $0.10 < z < 0.12$.

Gyrs) stars is 0.036 in red galaxies,⁸ and 0.019 in blue galaxies, which would suggest that the two form distinct populations.

Whatever the interpretation of the observations, it seems unlikely that they can be made compatible with the model galaxies, which show widely divergent SFHs for red and blue galaxies for stars younger than 5 Gyr. It would seem that termination of star-formation is too abrupt in the models as compared the observations, and lacks the possibility of retriggering of star-formation at later times.

The comparison of observed and model galaxies is complicated by the effects of metallicity, dust attenuation and finite fibre aperture on the measured colours. In the models, there is a very strong correlation between stellar mass and metallicity, and between SFR and extinction; in addition; there is no aperture correction. In real galaxies, the scatter is observed to be much higher, and there will be a redshift-dependent colour correction for the finite aperture. This, together with observational error, is likely to move the observed blue and red populations towards each other, so caution should be exercised before drawing definitive conclusions. On the other hand, SA models struggle to match even the colour distribution of galaxies (see, for example, Fig. 9 of HWT14), and the distinction between the models and the observed SDSS data is so large that it is hard to dismiss it lightly. This issue will be investigated in a subsequent paper, and highlights the power in comparing fully-resolved SFHs between models and data.

5 THE EVOLUTION OF STAR FORMATION HISTORIES

This section looks at the predicted SFHs of galaxies at different redshifts. We are interested both in the history of the mean (and median) galaxy population and of the scatter about that mean. This can have important implications for the interpretation of high-redshift galaxies that often rely upon postulated SFHs (Boquien et al. 2014; ?).

⁸ In units of the mass fraction of metals with respect to Hydrogen; in these units solar metallicity is $Z_{\odot} = 0.02$

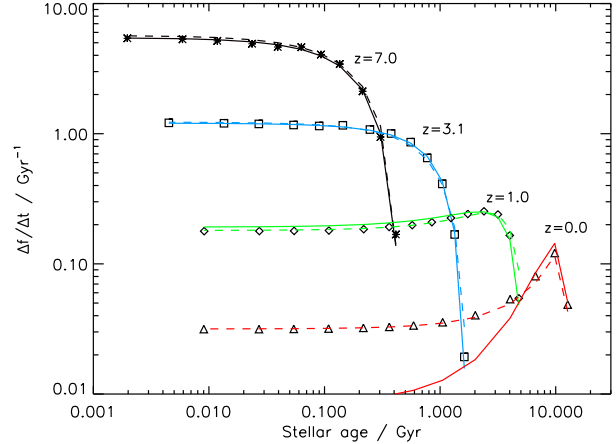


Figure 6. The average star formation rates of model galaxies from the HWT14 model, with mass greater than $10^{9.5} M_{\odot}$, at four different redshifts, as shown. The symbols show the model predictions; the curves are fits to the data as described in the text: solid lines, gamma model (Equation 1); dashed lines, two-power model (Equation 2).

5.1 Mean star-formation histories

Figure 6 shows the mean, mass-weighted star-formation rates (hereafter SFRs) of all galaxies with mass greater than $10^{9.5} M_{\odot}$ at four different redshifts: 0, 1, 3 & 7. (Note that this plot differs from previous ones in that we are plotting $\Delta f/\Delta t$ rather than $\Delta f/\Delta \log t$; we do this to make it easier to detect any decrease in the SFR at recent times). The SFR increases rapidly at early times, then slows down, with a decline to late times (i.e. low stellar ages) being apparent for $z \lesssim 2$.

To characterise the SFR at high redshift, we fit a gamma model featuring a power-law increase in star formation at early times followed by an exponential decline.⁹

$$\frac{df}{dt} = Ax^p e^{-x}, \quad x = \frac{t_a - t}{\tau}. \quad (1)$$

Here t_a is the age of the galaxy, p sets the rate at which star-formation builds up, and τ is the characteristic timescale over which star-formation declines.

At all redshifts above $z = 1$, the SFHs are well-fit by a single set of parameters, $p = 1.5$ and $\tau = 2.0$ Gyr, with only t_a varying to reflect the age of the galaxy.¹⁰ That this is the case is not surprising but reflects that fact that the majority of stars in the Universe are born within galaxies whose mass exceeds $3 \times 10^9 M_{\odot}$: each of the SFHs shown in Figure 6 then mirrors the cosmic SFH. Using this set of parameters then star-formation begins in our model at $z \approx 12$, 0.4 Gyr after the Big Bang, and levels off (i.e. $d^2 f/dt^2 = 0$) 3 Gyr later, at $z \approx 2$.

At lower redshifts, it becomes apparent that an exponential decline is too steep. Instead, a two-power model is preferred:

$$\frac{df}{dt} = \frac{A}{x^{-p} + x^q}, \quad x = \frac{t_a - t}{\tau}. \quad (2)$$

⁹ The same functional form with $p = 1$ was shown by Simha et al. (2014) to be a good fit to the individual SFHs of most of their galaxies in SPH simulations of galaxy formation.

¹⁰ For $z \gtrsim 2$ these parameters are degenerate, but we choose to freeze them at the values found at lower redshift.

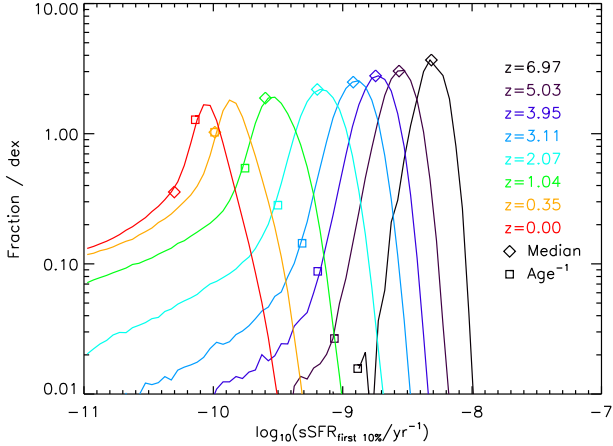


Figure 7. The specific star-formation rate at different redshifts for the HWT14 model. The subscript “first 10%” refers to an average over the most recent 10 per cent of the age of the Universe at that time. The diamonds show the median values and the squares show the inverse age of the Universe at each redshift.

Taking $p = 1.39$, $q = 1.33$ & $\tau = 3.0$ Gyr gives a good fit at all redshifts.

Behroozi et al. (2012) found identical fitting formulae to those used here to be good fits to the SFHs of galaxies in their abundance matching method to populate haloes with galaxies that match observed stellar mass functions and star-formation rates. However, for $10^{12} M_{\odot}$ haloes, they find a value of q , that determines the rate of decay of the SFR at late times, to be significantly higher than that quoted above: the reason for this difference is not clear.

We stress that the curves shown in Figure 6 are for the mean star-formation rate averaged over all galaxies with mass greater than $10^{9.5} M_{\odot}$. As is apparent from Figure 4, high mass galaxies form their stars earlier, and low mass galaxies later, than the mean trend. We show in Section 5.3 that this is driven primarily by a mass-dependence in the cessation of star-formation, and in Section 5.4 that there is considerable variation between individual galaxies.

5.2 Specific star-formation rates and quiescent fractions

Figure 7 shows the specific star-formation rate (sSFR) of all galaxies with $M > 3 \times 10^9 M_{\odot}$ in the HWT14 mode at several different redshifts. The star-formation rate here is averaged over the most recent 10 per cent of the age of the Universe at that time. The diamond symbols show the location of the median values, and the squares show the inverse age of the Universe at that redshift.

There is a small spread around the modal sSFR, with the vast majority of star-forming galaxies lying within about ± 0.25 dex of the peak. However, there is a long tail of galaxies extending to low sSFRs, which becomes more prominent at low redshifts; indeed, at $z = 0$, 35 per cent lie off the left-hand edge of the plot altogether. That is why, below $z = 1$, the median values lie well to the left of the mode.

Above $z \approx 0.35$, most galaxies are forming stars at a rate that would more than double their mass in the age of the Universe;¹¹

¹¹ Note that this is a number-weighted average, so that does not mean that mean star-formation rate peaked at that time.

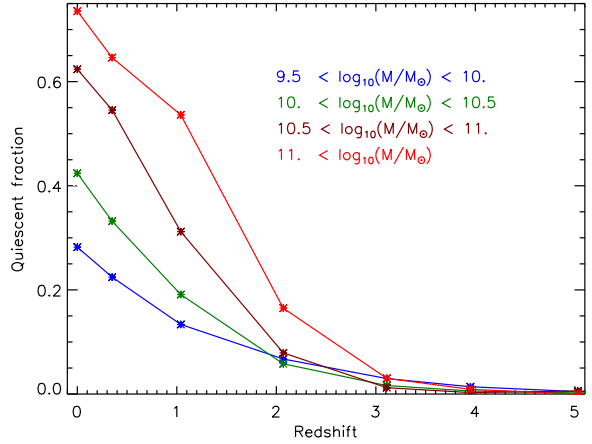


Figure 8. The quiescent fraction of galaxies in the HWT14 model, in several different mass bins, and at several different redshifts, as shown.

below that redshift, the opposite is true. It is at this time that there is a strong shift from star-forming to non-star-forming galaxies. There is no sharp distinction between the two but, using Figure 7 as a guide, we define a galaxy to be *quiescent* if it has formed fewer than 3 per cent of its stars in the most recent 10 per cent of the age of the Universe, t_z , at that redshift, i.e. $\text{sSFR}_{\text{first } 10\%} < 0.3/t_z$.

Figure 8 shows the fraction of quiescent galaxies as a function of mass and redshift. At high redshift, there is some suppression of star formation in dwarf galaxies, reflecting the strong feedback from supernova in the model. However, only a small fraction of galaxies are affected and there is a much greater growth of the passive population at redshifts below $z \approx 3$. Once again, there is clear evidence of down-sizing in that more massive galaxies start to become quiescent earlier than lower-mass ones.

Table 3 lists several measures of star-formation activity. $S_{0.5,\text{all}}$ is the median sSFR of the sample multiplied by the age of the Universe at that redshift; likewise $S_{0.5,\text{sf}}$ is the same thing, but restricted to star-forming galaxies. The two begin to differ significantly below a redshift of about 3 once the quiescent fraction begins to rise. This fraction is listed weighted both by galaxy number and by galaxy mass, from which it can be seen that about 58 per cent of stars in the current-day Universe lie in galaxies that are not actively star-forming.

The medians listed in the table show that there has been a steady decline in star-formation activity in galaxies from a redshift of at least 7 right through to the current day. However, even as recently as $z \approx 0.35$, most galaxies were still forming stars at a rate that would more than double their mass within the age of the Universe at that time.

5.3 The cause of mass-dependent star-formation histories

The top panel of Figure 9 shows the SFHs of galaxies at $z = 0$ split into 4 different mass bins. In order to better illustrate the onset of star-formation, which is poorly resolved at $z = 0$ using our default number of bins, for this section only we use $N_{\text{max}} = 4$ (see Section 2.3), giving 29 time bins at $z = 0$. Age down-sizing is clearly visible with more massive galaxies forming their stars earlier than lower-mass ones.

To better understand the cause of this, the middle and lower panels show the same curves for star-forming, and for quiescent

Table 3. The median specific star-formation rates, and the quiescent fraction of galaxies in the HWT14 model with mass exceeding $3 \times 10^9 M_{\odot}$. The columns are: redshift; age of the Universe in Gyr, t/Gyr ; median specific star-formation rate multiplied by the age of the Universe, $S_{0.5,\text{all}}$; ditto but restricted to star-forming galaxies, $S_{0.5,\text{sf}}$; quiescent fraction weighted by number, Q_{num} ; and quiescent fraction weighted by mass, Q_{mass} .

Redshift	t/Gyr	$S_{0.5,\text{all}}$	$S_{0.5,\text{sf}}$	Q_{num}	Q_{mass}
6.97	0.77	3.71	3.71	0.00	0.00
5.03	1.16	3.17	3.17	0.00	0.00
3.95	1.56	2.81	2.82	0.01	0.01
3.11	2.06	2.50	2.53	0.03	0.02
2.07	3.17	2.02	2.09	0.07	0.08
1.04	5.69	1.43	1.60	0.18	0.28
0.35	9.79	0.99	1.31	0.33	0.48
0.00	13.80	0.69	1.17	0.41	0.58

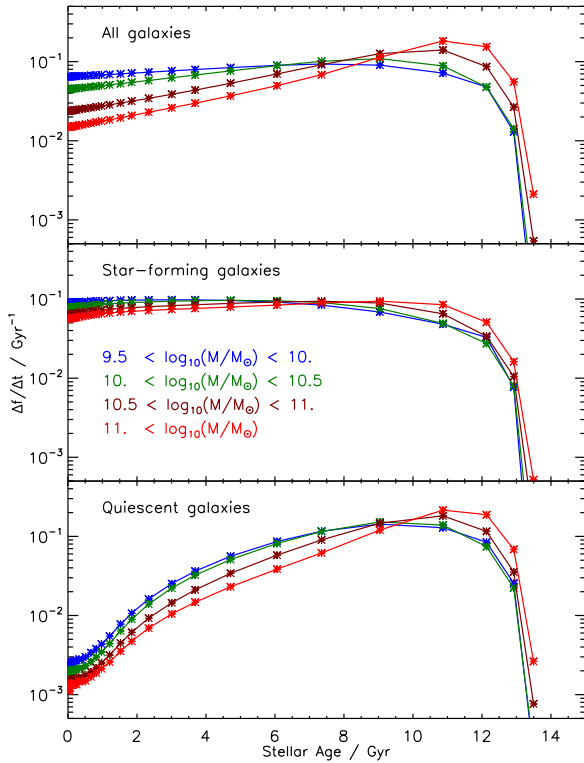


Figure 9. The star-formation rate as a function of time for the HWT14 model at $z = 0$, split into 4 different mass bins, as shown. The upper panel shows all galaxies in each mass-range; the middle panel shows star-forming galaxies; and the lower-panel panel shows quiescent galaxies, as defined in Section 5.2.

galaxies, respectively. Although the correspondence is not perfect, the agreement between the different mass-bins is much tighter in the central panel than in the upper one. That strongly suggests that the SFHs of star-forming galaxies are very similar, independent of the mass of the galaxy, and that the primary driver of the mass-dependence is the different evolution of the quiescent fraction. Note that we tried only a single definition of quiescence and it is likely that the residual mass-dependence in the central panel could be reduced even further if we optimised the definition for that purpose.

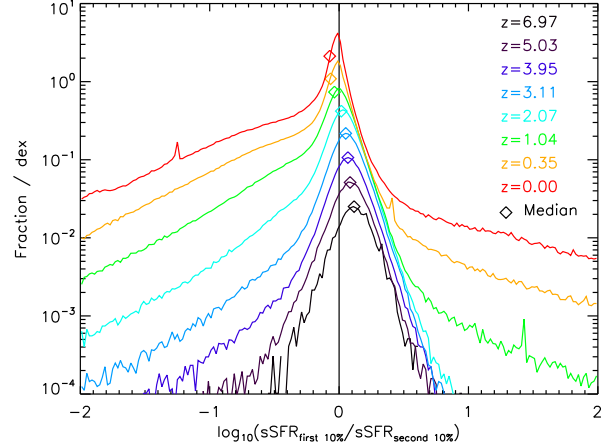


Figure 10. The ratio of the star-formation rate in the most recent ('first') 10 per cent, to that in the previous ('second') 10 per cent, of the age of the Universe at that redshift, for galaxies with masses exceeding $10^{9.5} M_{\odot}$ in the HWT14 model. The y -scale corresponds to the $z = 0$ curve: the higher-redshift curves are offset by successive factors of two to space them out in the y -direction. The diamond symbols show the median values.

5.4 Individual star-formation histories

In this section, we restrict our attention to star-forming galaxies.

Although the mean SFH is well-described by a simple functional form, Figure 10 shows that individual galaxies have a wide variety of histories. This figure shows histograms of the rate of decline of the star-formation rate measured by the ratio in two successive time bins: the most recent 10 per cent, and the next most recent 10 per cent, of the age of the Universe at that redshift. Galaxies to the left/right of the vertical line have declining/increasing star-formation rates, respectively.

The distribution of ratios is shown in Figure 10 for a variety of redshifts. There is a gradual shift from increasing to decreasing specific star-formation rates as the Universe ages. When measured in this way, an equal balance between increasing and decreasing star-formation rates is achieved somewhere between redshifts 1 & 2. At all times, however, there is a significant fraction of galaxies lying in each of these populations: at $z = 7$, four-fifths of galaxies show an increasing SFR, and at $z = 0$ three-quarters show a decreasing one.

6 CONCLUSIONS

In this paper, we have introduced the recording of star-formation histories (SFHs) in the L-GALAXIES SA model. At any given point in a galaxy's evolution, the mass of recently-formed stars is recorded in bins of time resolution equal to that of the time-step in the SA model ($1-2 \times 10^7$ yr). These bins are gradually merged together as the galaxy ages, such that older stars are grouped together into larger bins.

We investigate the extent to which SFHs may be used to reconstruct stellar spectra in post-processing; we compare our SFHs to those in the publicly-available VESPA catalogue extracted from SDSS-7 data; and we investigate in our favoured SA model (Henriques et al. 2014) the evolution of SFHs as a function of galaxy mass. Our key results are as follows:

- Post-processing reconstruction of magnitudes in various ob-

servational bands gives good agreement with on-the-fly accumulation of luminosity, provided that $N_{\text{merge}} \geq 2$ (which equates to ≥ 16 bins at $z = 0$). Quantitatively, the root-mean-square difference between raw and reconstructed magnitudes is less than 0.05 for all bands except the far-UV, for which it is 0.29.

- The SA models show reasonable qualitative agreement with the observed SFHs of the SDSS Main Galaxy Sample from the VESPA catalogue, with the GWB11 model fitting better for stars older than 1 Gyr, and the HWT14 model fitting better for younger stars.

- When divided the mass, both the observations and models show a trend for more massive galaxies to form their stars earlier and have lower current sSFRs than lower-mass galaxies.

- When divided by colour, the agreement is poorer. Both versions of the SA model show much more extreme variation in SFH with colour than do observed galaxies from the VESPA database. In the model, the SFHs of red and blue galaxies begin to differ as long ago as 5 Gyr, compared to just 0.3 Gyr for observed galaxies. One possible explanation could be that real galaxies show repeated episodes of star-formation that are not present in the models. We note, however, that a more rigorous investigation of the data is required before drawing any definitive conclusions.

- At $z \geq 1$ the mean star-formation rate (SFR) of all model galaxies with stellar mass greater than $3 \times 10^9 M_{\odot}$ is well-fit by the formula $df/dt \propto x^{1.5} e^{-x}$, where $x = (t_a - t)/2.0$ Gyr. Here t is the lookback time and t_a is the age of the galaxy. At later times, the SFR declines less rapidly and a two-power model (that contains an extra parameter) is a better fit over the whole of cosmic history: $df/dt \propto 1/(x^{-1.39} + x^{1.33})$, where $x = (t_a - t)/3.0$ Gyr.

- Although star-formation rates have been declining for more than half the history of the Universe, the typical (median) star-forming galaxy today is still forming stars at a rate that will more than double its mass in a Hubble time.

- We define a galaxy to be quiescent if it forms fewer than 3 per cent of its stars in the most recent 10 per cent of the age of the Universe, t_z at that redshift, i.e. $\text{sSFR} < 0.3/t_z$. Then the quiescent fraction begins to increase rapidly below $z \sim 3$, reaching 41 % by number and 58 % by mass for galaxies with $M > 10^9 M_{\odot}$ at the current day.

- Our model produces a small fraction of quiescent dwarf galaxies, $M < 10^{10} M_{\odot}$ at all times, but the main effect that we see is consistent with down-sizing in that more massive galaxies become quiescent first, followed by successively lower mass galaxies as the Universe ages.

- When split by mass, and using a finer time resolution in the SFHs, down-sizing is very clear to see, with the peak of the SFR shifting from a lookback time of about 11 Gyr in the most massive galaxies (current-day mass greater than $10^{11} M_{\odot}$) to less than 8 Gyr in lower-mass systems ($3 \times 10^9 - 10^{10} M_{\odot}$).

- When split into quiescent and a star-forming populations, the differences between the mean SFHs of star-forming galaxies of different mass is much reduced. Down-sizing thus has its origin in an earlier transition from star-forming to quiescent status in galaxies that are more massive at the current-day.

- Although the mean SFHs are well-defined, there is a huge dispersion in the SFHs of individual galaxies such that, even at the current day, many galaxies still have increasing SFRs. At $z = 7$, four-fifths of galaxies show an increasing SFR, and at $z = 0$ three-quarters show a decreasing one; an equal balance between galaxies with increasing and decreasing star-formation rates is achieved somewhere between redshifts 1 & 2.

As can be seen from the above, one of the key drivers of galaxy evolution is the rate at which star-formation is quenched. This is investigated in a companion paper, ?, that undertakes a detailed comparison with observations of the quenched fraction as a function of environment and mass. There it is shown that the HWT14 model does a much better job than previous incarnations of the L-GALAXIES SA model in terminating star-formation in massive galaxies, whilst allowing continued star-formation in low-mass satellites, though the quantitative agreement is still far from ideal.

An earlier paper, Yates et al. (2013), combined the star-formation histories with a multi-component model for stellar feedback to investigate the metallicity evolution of galaxies. This then enables us to construct metallicity histories for galaxies along the lines of the SFHs presented in this paper. Unfortunately, the observational data from VESPA is currently unable to constrain the metallicity histories with any degree of certainty.

The low-resolution ($N_{\text{max}} = 2$) SFHs for the HWT14 SA model, presented in this paper, are publicly available to download from the Millennium database¹² and have been used to reconstruct predicted fluxes in post-processing. Higher-resolution catalogues are available from the authors upon request.

ACKNOWLEDGEMENTS

The authors contributed in the following way to this paper. SS undertook the vast majority of the data analysis and produced a first draft of the paper and figures. PAT supervised SS, led the interpretation of the results, wrote the bulk of the text. BH led and wrote the section on post-processing of magnitudes. RT led the interpretation of the VESPA results. At different stages each of the other authors (excepting GL) were responsible for discussion of the results, shaping different parts of the paper, and helping to draft the text. GL provided the technical support to help integrate the post-processing of galaxy magnitudes in the Munich GAVO repository (aka the Millennium database).

This paper draws upon data from the VESPA database, hosted by the ROE. Much of the data analysis was undertaken on the COSMA-4 supercomputer at Durham and on the APOLLO cluster at Sussex.

PAT, SJO & SW acknowledge support from the Science and Technology Facilities Council (grant number ST/L000652/1). RT acknowledges support from the Science and Technology Facilities Council via an Ernest Rutherford Fellowship (grant number ST/K004719/1). GL was supported by Advanced Grant 246797 ‘‘GALFORMOD’’ from the European Research Council and by the National Science Foundation under Grant No. 1261715.

REFERENCES

- Angulo R. E., White S. D. M., 2010, *MNRAS*, 405, 143
 Angulo R. E., White S. D. M., Springel V., Henriques B., 2014, Galaxy formation on the largest scales: the impact of astrophysics on the baryonic acoustic oscillation peak
 Behroozi P. S., Wechsler R. H., Conroy C., 2012
 Boquien M., Buat V., Perret V., 2014, *A&A*, submitted, astro-ph/1409.5792

¹² <http://gavo.mpa-garching.mpg.de/MyMillennium/>

- Boylan-Kolchin M., Springel V., White S. D. M., Jenkins A., Lemson G., 2009, Resolving Cosmic Structure Formation with the Millennium-II Simulation
- Bruzual G., Charlot S., 2003, MNRAS, 344, 1000
- Calzetti D., 1999, ApSS, 266, 243
- Cid Fernandes R., Gu Q., Melnick J., Terlevich E., Terlevich R., Kunth D., Rodrigues Lacerda R., Joguet B., 2004, MNRAS, 355, 273
- Cid Fernandes R., Mateus A., Sodré L., Stasińska G., Gomes J. M., 2005, MNRAS, 358, 363
- Cohn J. D., van de Voort F., 2014
- Collaboration P., et al., 2013, A&A, submitted
- Guo Q., White S., Boylan-Kolchin M., Lucia G. D., Kauffmann G., Lemson G., Li C., Springel V., Weinmann S., 2011, MNRAS, 413, 101
- Heavens A., Panter B., Jimenez R., Dunlop J., 2004, Nat., 428, 625
- Henriques B., White S., Thomas P., Angulo R., Guo Q., Lemson G., Springel V., 2013, MNRAS, 431, 3373
- Henriques B., White S., Thomas P., Angulo R., Guo Q., Lemson G., Springel V., Overzier R., 2014, MNRAS, submitted, astro-ph/1410.0365
- Kennicutt Jr. R. C., 1998, ARA&A, 36, 189
- Koleva M., Prugniel P., Bouchard A., Wu Y., 2009, A&A, 501, 1269
- Maraston C., 2005, MNRAS
- Ocvirk P., Pichon C., Lançon A., Thiébaud E., 2006, MNRAS, 365, 46
- Panter B., Heavens A. F., Jimenez R., 2003, MNRAS, 343, 1145
- Panter B., Jimenez R., Heavens A. F., Charlot S., 2007, MNRAS, 378, 1550
- Simha V., Weinberg D. H., Conroy C., Dave R., Fardal M., Katz N., Oppenheimer B. D., 2014
- Springel V., White S. D. M., Jenkins A., Frenk C. S., Yoshida N., Gao L., Navarro J., Thacker R., Croton D., Helly J., Peacock J. A., Cole S., Thomas P., Couchman H., Evrard A., Colberg J., Pearce F., 2005, Nat., 435, 629
- Tojeiro R., Heavens A. F., Jimenez R., Panter B., 2007, MNRAS, 381, 1252
- Tojeiro R., Masters K. L., Richards J., Percival W. J., Bamford S. P., Maraston C., Nichol R. C., Skibba R., Thomas D., 2013, MNRAS, 432, 359
- Tojeiro R., Wilkins S., Heavens A. F., Panter B., Jimenez R., 2009, ApJS, 185, 1
- Yates R. M., Henriques B., Thomas P. A., Kauffmann G., Johansson J., White S. D. M., 2013, MNRAS, 435, 3500

APPENDIX A: THE CHOICE OF VESPA CATALOGUE

The VESPA SDSS-7 catalogue (Tojeiro et al. 2009) contains galaxies with a wide variety of data quality, some showing reconstructed mass errors that are greater than 100%. In order not to bias the results, we include the whole sample in our analysis. When show average star-formation histories weighted by galaxy number, rather than galaxy mass, so as to minimise the effect of the errors in the mass reconstruction. We have checked that restricting the analysis to the galaxies with the best data quality does, in fact, lead to qualitatively similar SFHs.

The average star-formation histories of galaxies in this sub-sample, weighted by galaxy number, are shown in Figure A1 for two different SEDs (Bruzual & Charlot 2003, hereafter BC03 and

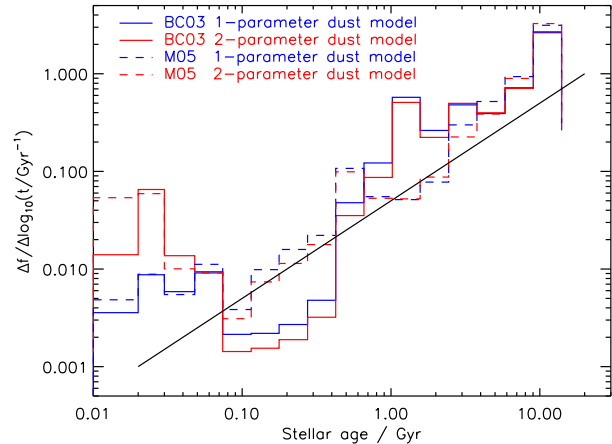


Figure A1. The average star formation history of VESPA galaxies obtained using the SEDs of BC03 (solid lines) and M05 (dashed lines). Blue lines show results for a one-parameter dust model whereas red shows a two-parameter dust model. The solid, black line has a slope of unity, corresponding to a constant star-formation rate.

Maraston 2005, hereafter M05) and two different dust models. The one-component dust model is a uniform screen applied to the whole stellar population; the two-component model adds in extra absorption in front of young stars.

First note that the M05 models show a much smoother change in the star-formation rate between look-back times of 0.1-10 Gyr than do those of BC03. In such a large galaxy sample, it is hard to think of a plausible reason for this and the SA models show no such feature. For that reason, we use the M05 results.

Both the BC03 and, to a lesser extent, the M05 results for the 2-dust model show a significant increase in star-formation rate at ages less than 0.1 Gyr. Again, this seems implausible and suggests that there is not enough constraining power in the data: the model has presumably confused dust-obscured, young stars with some older population, perhaps to explain some spectral feature that is not well fit by the SEDs.

Throughout the body of the paper, we use the VESPA results for M05 and a single dust model.